Universidad de Zaragoza

Trabajo de Fin de Master

Curso 2024/2025

Quantum spin liquid phases in novel molecular materials

Author:

Chiara Speca

Tutor:

Fernando Luis Vitalla

Contents

CHAPTER 1

Introduction

Quantum computation requires controlled systems capable of addressing two main challenges: noise and decoherence. Isolating the quantum computer from the environment is essential to mitigate noise and to apply effective quantum-error correction protocols; remarkable results have been made in this direction. An alternative approach to *fault-tolerant quantum computation* is *topological quantum computation*.

It relies on objects called "non-Abelian anyons" to encode and manipulate quantum information non-locally. This non-locality makes the topological quantum computation immune to noise and decoherence [1].

Let's think about a solid state platform, where the lattice follows a well defined geometric pattern but the spins are correlated in such a way that the ground state behaves as a liquid. Imagine to be able to control, modify and detect these states by safely keeping their properties because of the nature of the system itself. For example by coupling these spin ensembles with a superconducting microwave resonator, we could have a stable platform on which to send pulses and efficiently manipulate qubits [2].

Theoretically, by controlling non-Abelian states, qubits can be initialized in well-defined states, unitary gates (such as the Hadamard, $\pi/8-$phase, and controlled-Z gates) can be implemented to form a universal gate set, and "fusion outcomes" of anyons could be measured post-computation [1]. In other words, manipulating non-Abelian anyons and measuring their states in controlled experiments could bring to the realization of a *topological quantum computer*.

The simplest realization of non-Abelian anyons are quasiparticles called Majorana fermions. These are believed to occur in a variety of solid state systems, such as topological superconductor, and in a variety of topological phases [3]. In particular, those quasiparticle excitations are a peculiar

feature of *Quantum Spin Liquids* [4][5], which are the focus of this work.

A *Quantum Spin Liquid* (QSL) is a state of matter characterized by the absence of long-range magnetic order, even at 0 K, while having a strong short-range antiferromagnetic interaction between spins [6]. Because of this disordered ground state, their spins are constantly in a flux, but they remains nevertheless correlated, like the molecules of a liquid [4]. This phenomenon, theorized for the first time by Anderson in 1973 [7], has its origin in the magnetic frustration of the spins that creates quantum fluctuations. So, even if the spins are long-range entangled, their magnetic ordering is destroyed by fluctuations.

Besides the implications in fundamental physics (the existence of quasiparticle excitation like Majorana fermions and the physics behind strongly correlated systems, like high-temperature superconductor), Quantum Spin Liquids could also provide a natural platform for quantum communication and topological quantum computation [6]. That is why the interest and the experimental research has growth in recent years, but the identification of a material with a Quantum Spin Liquid phase remains challenging. The goal of this work is to characterize two materials, $(PNP)ZnRu(ox)_3$ and $FeCpZnRh(ox)_3$, in order to understand if they could be good candidates for embodying a model realization of a Quantum Spin Liquid: the Kitaev model.

In the following chapters, I first describe the experimental methods and instruments used in this thesis; then I illustrate the main theoretical background of Quantum Spin Liquids, in particular the Kitaev model, and how to experimentally identify (or design) them. Then, one chapter is dedicated to the results we obtained and their discussion and finally the conclusions.

CHAPTER 2

Experimental methods

2.1 Samples

The compounds that have been studied in this work were synthesized by the group of Miguel Clemente from the Molecular Science Institute (ICMol) at the University of Valencia (Valencia, Spain). They were characterized by elemental analysis and by X-ray diffraction in order to determine its composition and the crystal structure.

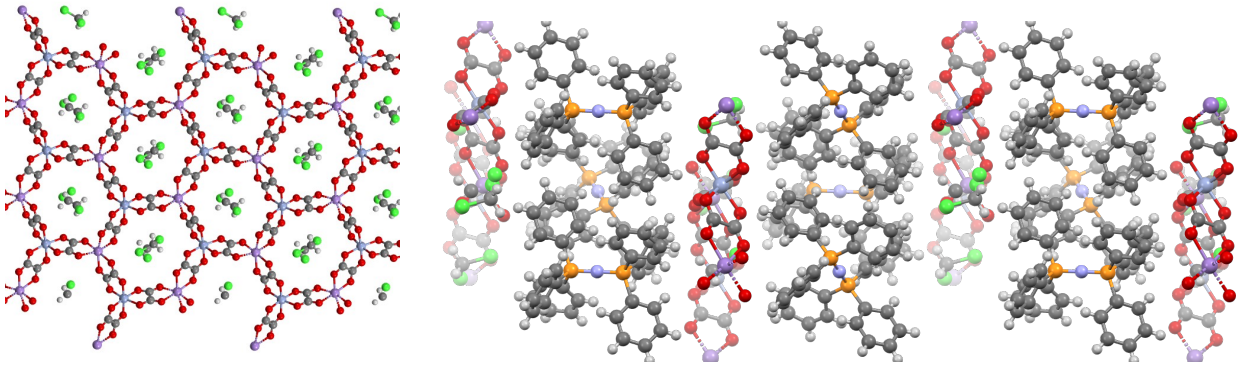

Figure 2.1: Left image: top-view of the $(PNP)ZnRu(ox)_3$. The oxalate-based lattice contains the Zn and Ru ions (purple and green), that alternate in a triangular lattice. Right image: side-view of the $(PNP)ZnRu(ox)_3$. The oxalate layers and the non-magnetic organic layers are alternating in such a way that the spin lattice is 2D

The $(PNP)ZnRu(ox)_3$ ($C_{43}H_{32}Cl_2ZnRuNO_{12}P_2$, molar mass: 1054.02 g/mol) is made of oxalate-based bimetallic layers separated by non-magnetic organic PNP layers. In this configuration the magnetic ions lie within a 2D lattice. The oxalate layer is made by Zn (diamagnetic) and Ru (paramagnetic) ions that alternate in a hexagonal lattice, thus the spin lattice, defined by the

nodes occupied by the Ru ions, is triangular (see Fig. 2.1).

The $FeCpRhZn(ox)_3$ ($Fe(C_{10}H_{15})_2ZnRh(C_2O_4)_3$, molar mass: 758.62 g/mol) incorporates the magnetic component into the layers intercalated between the oxalate ones. The latter are here diamagnetic. Yet, they form a sort of mould on which the ferrocene ($FeCp$) molecules have to accommodate. The latter then also form a triangular lattice (Figure 2.2).

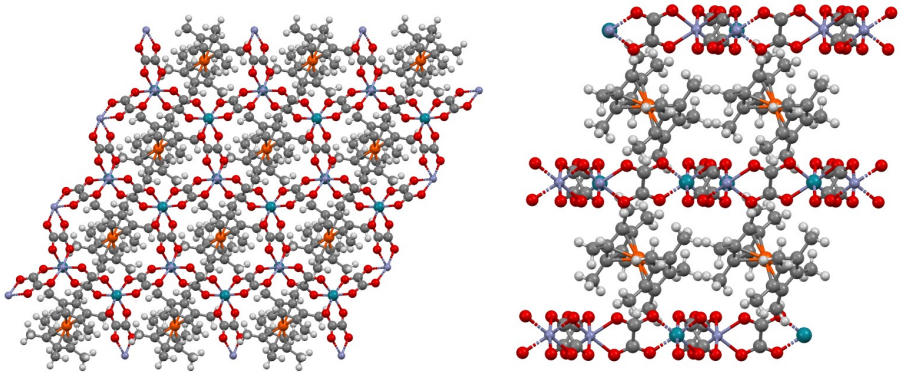

Figure 2.2: Top-view (left) and side-view (right) of the $FeCpRhZn(ox)_3$. The oxalate-based lattice (red and grey) with the Rh and Zn ions (purple and green) forms a structure to host the $FeCp$ molecules (yellow, grey and white).

These materials then provide two realizations of a hexagonal spin lattice, but with spins linked by different bridges, thus likely leading to spin-spin interactions of different strength and of a different nature.

2.2 Magnetic characterization experiments: SQUID magnetometry

Magnetic susceptibility experiments are performed with the Magnetic Properties Measurement System (MPMS - 3) operated by the Physical Measurements Service ("Servicio de medidas físicas - SMF") of the University of Zaragoza. This is a commercial magnetometer by Quantum Design based on a DC-SQUID detector (Figure 2.3 a)). It can perform measurements, like DC magnetization and AC susceptibility. Its high sensitivity allows measuring the magnetization of small samples in a wide temperature range, 0.4 K $< T <$ 300 K, thanks to a liquid He cryostat and another additional ^{3}He cryostat insert. The system includes a superconducting magnet that enables applying DC magnetic fields up to 7 T.

SQUIDs (Superconducting Quantum Interference Device) magnetometers are very sensible flux-to-voltage converters. In this MPMS, the SQUID is connected to a superconducting gradiometer, made of four coils placed one above the other with the two central coils wound in the opposite direction to the external coils (Figure 2.3 b)). This configuration cancels any contribution to the signal from the static external magnetic fields. The sample is inserted into a thin rod which is introduced inside the gradiometer and can travel along its full length (3 cm).

For DC measurements (DC susceptibility and magnetization), temperature and magnetic field

are fixed, and the system measures the output voltage of the SQUID as a function of the sample position in the gradiometer. The induced magnetization of the sample M produces a change in the magnetic flux across the coils, proportional to M [8, 9].

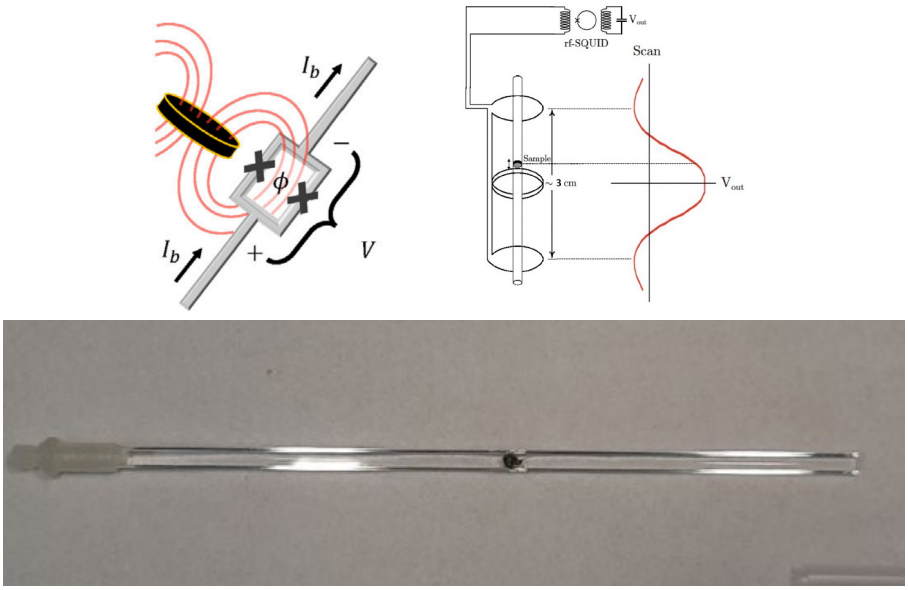

Figure 2.3: *a) Scheme of the SQUID-DC sensor. b) Scheme of the MPMS pick-up coil and its coupling to the SQUID sensor. c)* $(PNP)ZnRu(ox)_3$ *sample on the quartz rod.*

Preparation of the samples

The same procedure has been used both for $(PNP)ZnRu(ox)_3$ and $FeCpRhZn(ox)_3$, the two materials come in the form of a powder. They have been mixed with a *Apiezon N* grease, whose diamagnetic susceptibility has been determined in previous experiments: $\chi_d = -1.015 \times 10^{-6} \frac{\text{emu}}{\text{g Oe}}$.

The grease prevents the powder from moving inside the sample holder and it helps thermalizing it to the system temperature. Their masses has been determined with a scale having a 0.01 mg accuracy. For the $(PNP)ZnRu(ox)_3$ we determined: $m_{powder} = 1.31$ mg and $m_{Apiezon} = 2.79$ mg; for the $FeCpRhZn(ox)_3$: $m_{powder} = 4.42$ mg and $m_{Apiezon} = 5.02$ mg. The final mixtures were put on a sample holder made of quartz (Figure 2.3 c)), which is inserted inside a plastic straw and fixed to the thin rod that goes vertically inside the cryostat. However, the whole process, especially placing the mixtures on the sample holder, could have caused some losses from the original samples and therefore non-negligible errors in the mass estimation of the grease. As we will see in section 4.1 and Appendix A, a correction was necessary.

2.3 Heat capacity experiments

The heat capacity measurements are conducted with the Physical Properties Measurement System (PPMS) by Quantum Design, also available at the Physical Measurements Service of the University of Zaragoza. It can measure heat capacity while varying temperature and magnetic field.

As with the SQUID magnetometer, a combination of a liquid Helium cryostat and a ^{3}He insert give access to experiments between 350 mK and temperatures above room temperature. The system used for this thesis, includes a 14 T magnet.

The calorimeter is made of a sapphire sample holder, which is supported by 4 thin Au wires, that provide both thermal and electrical contact to the heater and the thermometer (Figure 2.4 a)). This configuration is the thermal equivalent of a RC circuit, which allows us to conduct very precise measurements using the thermal relaxation method. A square heat power P_{heater} (current I applied to the heater) pulse is applied for a controlled period of time and the calorimeter temperature is monitored as a function of time; when this input is removed, the sample slowly goes back to the bath temperature, which is fixed. The decay of the temperature is exponential in both cases, provided that the sample is in good thermal contact with the calorimeter and that it remains in thermal equilibrium. The decay time constant τ is directly related to the heat capacity C and the thermal conductivity K of the sample and the calorimeter [8]. Using the analogy with the electric circuit, the temperature evolution, equivalent to that of voltage in the RC circuit, can be written as:

$$T(t) - T_B = \frac{P}{K}(1 - e^{-t/\tau}); \quad \tau = C/K \tag{2.3.1}$$

This technique assures a higher sensitivity than other methods, like adiabatic calorimetry, because it performs time measurements.

Figure 2.4: a) Calorimeter scheme [8]. b) Sample assembly station. c) $(PNP)ZnRu(ox)_3$ tablet installed on the calorimeter and its holder frame. d) Calorimeter assembled on the probe of the cryostat.

Preparation of the samples

The $(PNP)ZnRu(ox)_3$ and the $FeCpRhZn(ox)_3$ cannot be used in the form of powder in the calorimeter. For this reason they were compressed in order to form a little pellet (respectively of 0.8 mg and 0.65 mg). The same grease *Apiezon N* used for the magnetic experiments, was used to fix

and thermalize the sample to the calorimeter platform.

In order to mount the sample on the calorimeter, the latter is placed on a platform (Figure 2.4 b)) that ensures that the small sapphire island supported by the 4 wires does not move and it is not damaged.

CHAPTER 3

Theoretical framework

Accurate theoretical modeling of the QSL properties is challenging because electrons in these systems are strongly correlated, which render single-electron approximations inapplicable. A notable exception is the Kitaev model, an exactly solvable framework that serves as a key tool for experimental investigations [4]. While numerous models have been developed in recent years, their connection to experiments remains limited. Consequently, many researchers rely on phenomenological low-energy theories to describe their equilibrium and dynamical responses [7].

In this chapter, we summarize the key theoretical frameworks that underpin our discussion and outline how to identify measurable quantities that may offer insights into the detection of a QSL.

3.1 Paramagnetic Spins

One of the main properties to look for in order to identify a possible QSL is the lack of a long-range magnetic order even at the lowest attainable temperatures. The lack of magnetic order leads to a close to paramagnetic behaviour. Here, we recall the basic models for simple paramagnets, and then introduce the effect of spin-spin interactions in the next section.

The Hamiltonian of a spin interacting with an external magnetic field is given by the Zeeman term [10]:

$$\mathcal{H}_0 = -\mu_B \vec{S} \hat{g} \vec{B} \tag{3.1.1}$$

where $\vec{S} = \frac{\hbar}{2}(\sigma_x, \sigma_y, \sigma_z)$ for a spin-1/2 system; $\mu_B = \frac{e\hbar}{2mc}$ is the Bohr magneton and $\hat{g} = \begin{pmatrix} g_x & 0 & 0 \\ 0 & g_y & 0 \\ 0 & 0 & g_z \end{pmatrix}$,

is the g-tensor, which parametrizes the effect of a magnetic field on the spin energy levels. The different principal values, g_x, g_y and g_z, account for the magnetic anisotropy, i.e. for the different coupling of the spins to magnetic fields applied along different directions of the crystal lattice.

Paramagnetism can be described through the **magnetization density M** ($M(H) = -\frac{1}{V}\frac{\partial E(H)}{\partial B}$). In particular, for a close to isotropic, S = 1/2 paramagnet, $M \approx N_A g \mu_B Stanh(\frac{g\mu_B S}{k_B T})$ [10], where g is an effective average factor. .

For sufficiently low fields, $M = \chi B$, where χ is the **magnetic susceptibility**; it is small, positive and strongly temperature dependent, according to the Curie Law $\chi = \frac{C}{T}$, where C is the Curie constant. For anisotropic spins the susceptibility is $\chi = \frac{1}{3}(\chi_{xx} + \chi_{yy} + \chi_{zz})$, where $\chi_{ii} \approx N_A \frac{g_i^2 \mu_B^2 S(S+1)}{3k_B T}$ ($k_B T >> g_i \mu_B H$) and g_i is the value from the $\hat{g} - tensor$. Any deviation from that behavior may indicate a ferromagnetic or antiferromagnetic interaction.

Studying the *heat capacity* reveals crucial information about the energy levels of magnetic systems. The heat capacity of a solid comes from different contributions like lattice vibrations and spin-spin interactions [11]. Isolating these contributions is key to a deeper understanding of the spin behavior.

For the phonon contribution we can refer to the Debye model ($\frac{c_D}{R} = aT^3$) [12], or the more general equation [11]:

$$\frac{c_D}{R} = 9\left(\frac{T}{\Theta_D}\right)^3 \int_0^{\frac{\Theta_D}{T}} \frac{xe^x}{(e^x - 1)^2} dx \tag{3.1.2}$$

Note that this behavior is independent of magnetic field, as it comes from the lattice vibration (associated to the thermal energy) [12]. This contribution decreases with temperature. Therefore, to make the phonon contribution negligible, we need to go to very low temperatures.

The specific heat of a paramagnetic S-1/2 system in an external magnetic field can be modeled using the Schottky anomaly characteristic of a two-level quantum system [11]:

$$C_S = N_A \frac{\Delta^2}{k_B T^2} \frac{e^{\frac{\Delta}{k_B T}}}{(1 + e^{\frac{\Delta}{2k_B T}})^2} \tag{3.1.3}$$

where Δ is the energy gap between the "ground " and the "excited" levels. For the experimental analysis, it will be useful to define this parameter in Kelvin: $T_\Delta = \frac{\Delta}{k_B}$ [13].

According to the Zeeman effect, the splitting of the energy levels is proportional to the applied magnetic field: $\Delta = g\mu_B B$, where g is the Landé g-factor and μ_B is the Bohr magneton.

3.2 Effect of spin-spin interactions on a paramagnetic state

In QSLs, spin-spin interactions are crucial and they need to be considered when analyzing the material's properties. A straightforward approach to modeling these interactions is through the *exchange Hamiltonian* from the Heisenberg model:

$$\mathcal{H}_{ex} = -\sum_{i<j} J_{ij} \vec{S}_i \cdot \vec{S}_j \tag{3.2.4}$$

where J_{ij} are the exchange coupling parameters [14].

This model leads to long-range magnetic order below a critical temperature T_c. Then, the spin-spin interactions become stronger than the thermal fluctuations, so they start to align. For $T > T_c$ the system remains paramagnetic but interactions affect the magnetic response and the specific heat. Since $T_c \longrightarrow 0$ in QSLs, as a first approximation we can study them as materials that are still in the paramagnetic region, above the critical temperature. The magnetic susceptibility can be computed with the Curie-Weiss Law:

$$\chi = \frac{N_A g^2 \mu_B S(S+1)}{3k_B(T-\Theta)} \tag{3.2.5}$$

where Θ is the Weiss temperature that parametrizes the effect of interactions. These interactions induce short range correlations between the spins. Then, flipping one of them costs energy even at $B = 0$. As a first approximation, C_P then has a nonzero magnetic contribution that depends on temperature as $C_p \propto T^{-2}$, similarly to what the Schottky anomaly, given by Eq.(3.1.3), does for $T > T_\Delta$. We can then assign a zero field energy excitation gap Δ_0 to introduce interactions in this equation, such that $\Delta \simeq \Delta_0 + g\mu_B B$.

3.3 Kitaev model

The model proposed by Kitaev in 2006 [15] provides a gold standard for the study of QSL. It describes a two-dimensional system of 1/2-spins on a honeycomb lattice (Figure 3.1). Its Hamiltonian describes nearest-neighbor Ising exchange interactions between spins located at different lattice nodes.

$$\mathcal{H} = -J_{xx} \sum_{<ij>_x} \hat{\sigma_i}^x \hat{\sigma_j}^x - J_{yy} \sum_{<ij>_y} \hat{\sigma_i}^y \hat{\sigma_j}^y - J_{zz} \sum_{<ij>_z} \hat{\sigma_i}^z \hat{\sigma_j}^z \tag{3.3.6}$$

where $\hat{\sigma_i}^{x,y,z}$ are the Pauli matrices and $< ij >_{x,y,z}$ are the sites sharing the strong anisotropic bond along each lattice direction. These anisotropic interactions cause a strong quantum frustration. The model's exact solution shows a ground state with no long range order down to $T = 0$ K and excitations that are Majorana fermions. Depending on the relative values of J_{xx}, J_{yy} and J_{zz}, two distinct phases can be generated: gapless and gapped quantum spin liquids [4, 5].

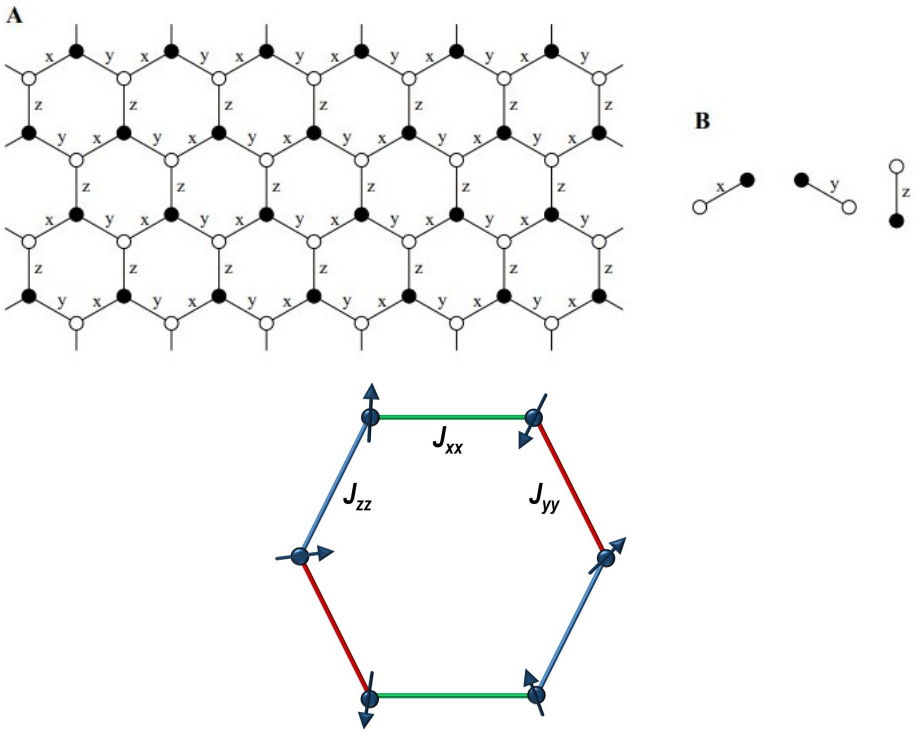

Figure 3.1: Upper image: Honeycomb lattice (A) with three types of links: x, y and z (B) [15]. Lower image: Graphic representations of Hamiltonian (3.3.6)

In real materials, Kitaev-like interactions coexist with Heisenberg-like interactions. A *Generalized Kitaev-Heisenberg model* was introduced in reference [16], it provides useful indications on how to recognize a QSL experimentally. Its basic Hamiltonian is:

$$\hat{\mathcal{H}}_{CJK} = \sum_{\Gamma=X,Y,Z} \sum_{<i,j>\in\Gamma} \vec{S}_i^T \mathcal{J}_\Gamma \vec{S}_j \tag{3.3.7}$$

where the matrix of exchange coupling tensors along different lattice bonds are defined as:

$$\mathcal{J}_X = \begin{bmatrix} K+J & 0 & 0 \\ 0 & J & 0 \\ 0 & 0 & J \end{bmatrix}, \quad \mathcal{J}_Y = \begin{bmatrix} J & 0 & 0 \\ 0 & K+J & 0 \\ 0 & 0 & J \end{bmatrix}, \quad \mathcal{J}_Z = \begin{bmatrix} J & 0 & 0 \\ 0 & J & 0 \\ 0 & 0 & K+J \end{bmatrix}. \tag{3.3.8}$$

Here, $K = 2Asin\varphi$ and $J = Acos\varphi$ are the Kitaev and Heisenberg coupling constants, respectively; where A has the dimension of energy and φ is a control parameter. The ground state of this model ranges from trivial magnetically ordered states to the QSL state, which occurs for $\varphi \sim 90°$ and $\varphi \sim 270°$. The model has been solved by quantum Monte Carlo calculations, described in Ref. [16]. A key prediction is that the exponent of c_P vs T is not necessarily -2. Indeed, as we can see from Figure 3.2, the specific heat shows no sharp peak or anomaly marking the onset of long-range magnetic order but, instead, two peaks at temperatures T_L and T_H, which mark the progressive population of low-energy and high-energy Majorana fermions.

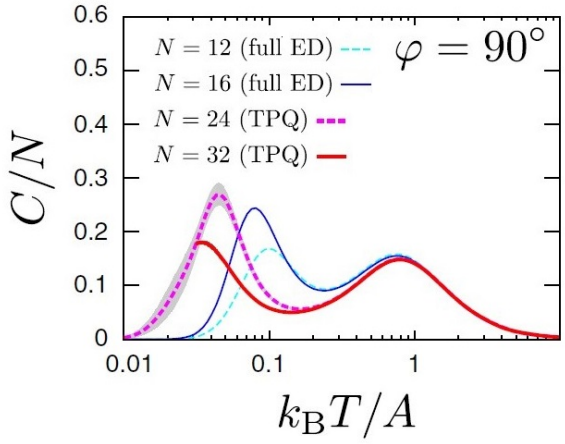

Figure 3.2: Temperature dependence of the specific heat C of the generalized Kitaev-Heisenberg model $\hat{H}_{CJK}$ obtained by numerical simulations on lattices of different number of nodes N. The Kitaev's QSL phase is identified with $\varphi = 90°$; it has two peaks in the temperature dependences of C. Adapted from [16].

The entropy at temperatures between the two peaks is an indicator of the proximity to the Kitaev QSL state [16]. Indeed, as shown in Ref. [17], a system with a Kitaev QSL ground state shows a half plateau in S, between the temperatures of the two peaks of C, with a value $(Nk_B/2)ln2$. This value is an indication of a Kitaev QSL model and the systems close to it.

3.4 Experimental realization of a Kitaev Spin Liquid

Metal-organic frameworks (MOFs) are promising candidates for the realization of a Kitaev QSL. First, and as it was introduced in section 2.1, the magnetic ions organize in a 2D hexagonal lattice. Besides, they have three main advantages: the suppression of direct exchange interaction (which is strong in inorganic materials between the metal ions), the flexibility in designing the parameters by choosing different ligand molecules, and the natural realization of complex structures.

However, the main distinctive feature for this work is that ab initio calculations performed for such frameworks [18] show that interactions between nearest neighbour spins can be described with the generalized Heisenberg Kitaev model described above. Even more, thanks to the existence of destructive interference between different superexchange paths, it is found that the ratio K/J becomes very small when the nodes are occupied by ions with a very strong spin-orbit coupling. In particular, $K/J < 10^{-3}$ is predicted in the case of Ru. This has inspired the choice of one of the materials studied in this work.

CHAPTER 4

Experimental results and discussion

4.1 Magnetic characterization experiments: SQUID magnetometry

The MPMS-3 led to two kinds of data.

- Magnetic susceptibility χ (emu/Oe) in a temperature range of 2K - 300K, at a fixed magnetic field $B = 0.1$ T.
- Magnetization M (emu) in a magnetic field range of 0 Oe - 70×10^3 Oe at different fixed temperatures ($T = 50$ K, 40 K, 30 K, 20 K, 10 K, 7 K, 5 K, 2 K).

Afterwards we repeated the same measurements with the ^3He cryostat that gives access to the temperature range of 0.360 K - 3 K. The magnetic susceptibility and the magnetization data shown below (except for the raw data) are intended as molar quantities.

4.1.1 Determination of the intrinsic magnetic response of the samples

In this section, we describe how the magnetic data were analyzed in order to extract from them the intrinsic paramagnetic contribution from the samples. We illustrate the method with data measured on the $(PNP)ZnRh(ox)_3$ sample.

Figure 4.1 shows the raw magnetic data measured between 2 K and 300 K. They follow a paramagnetic behavior, except for the fact that the magnetization M becomes negative at high T.

A first correction attempt was made by removing the diamagnetic contribution from the grease

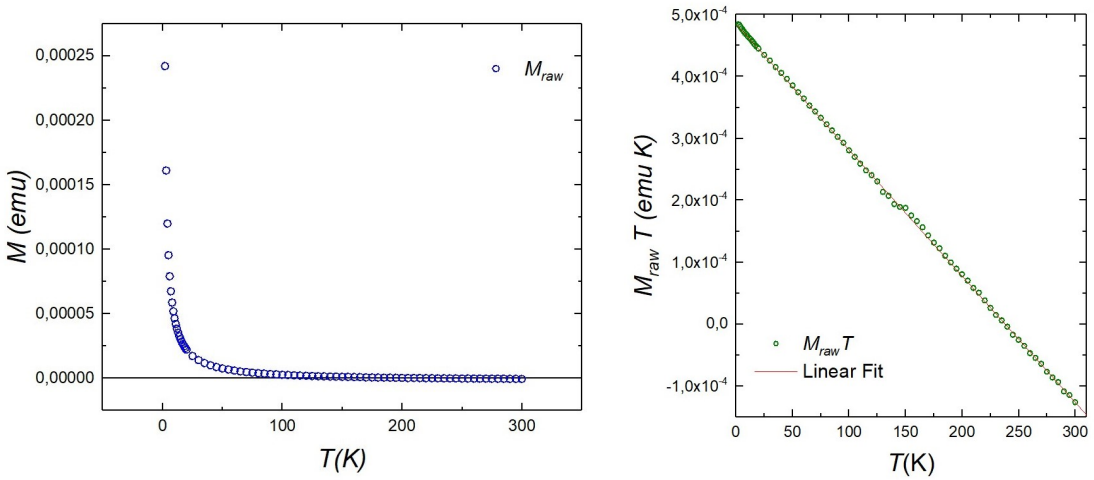

Figure 4.1: Raw magnetization data measured on $(PNP)ZnRu(ox)_3$. a) M_{raw} vs T plot seems to follow the Curie Law but it is going towards negatives values. b) $M_{raw}T$ vs T plot, from the slope of the linear fit we can derive the diamagnetic contribution.

as follows.

$$M_{mol} = (M_{measured} - \chi_{\rm d} m_{Apiezon} B)\frac{m_{molar}}{m_{sample}}; \quad \chi_{mol} = M_{mol}/B \tag{4.1.1}$$

where $\chi_{\rm d}$ and $m_{\rm Apiezon}$ are, respectively, the diamagnetic susceptibility and the mass of the grease. However, this correction was not accurate enough, because of some error in the estimation of the mass during the sample's preparation process. Besides, the diamagnetism comes from the grease (*Apezon N)*, heavily present in the sample mixture, but also from the experimental environment and the crystal lattice.

In order to circumvent these problems, we tried a different method, which aims to estimate the diamagnetic contribution from the whole magnetization. For this, we plot MT. Since the paramagnetic contribution is $\sim C/T$, especially at high temperatures, $MT \simeq M_{\rm dia}T + C$, with $M_{\rm dia} < 0$, as observed experimentally (Fig. 4.1, right). The fit gives $M_{\rm dia} = -2.04 \times 10^{-6}$ emu. Both procedures are described in detail in Appendix A.

The molar susceptibility obtained by this method (Fig. 4.2) suggests a Curie-Weiss behavior, with a Weiss temperature $\Theta = 0.15$ K. These data are measured only down to 2 K. Therefore they provide a good estimation of the Curie constant ($C = 0.5$ emu K / Oe mol) but Θ needs to be refined with data at lower temperatures.

4.1.2 Scaling of very low-T data

In order to add the data obtained with the SQUID ^3He insert to the analysis, we need to rescale them with the ones obtained at higher T, already corrected from diamagnetic contributions (the ones in Figure 4.2). This is necessary because the two measurements were done with a different experimental setup and different experimental conditions. In particular, the ^{3}He insert has an extra

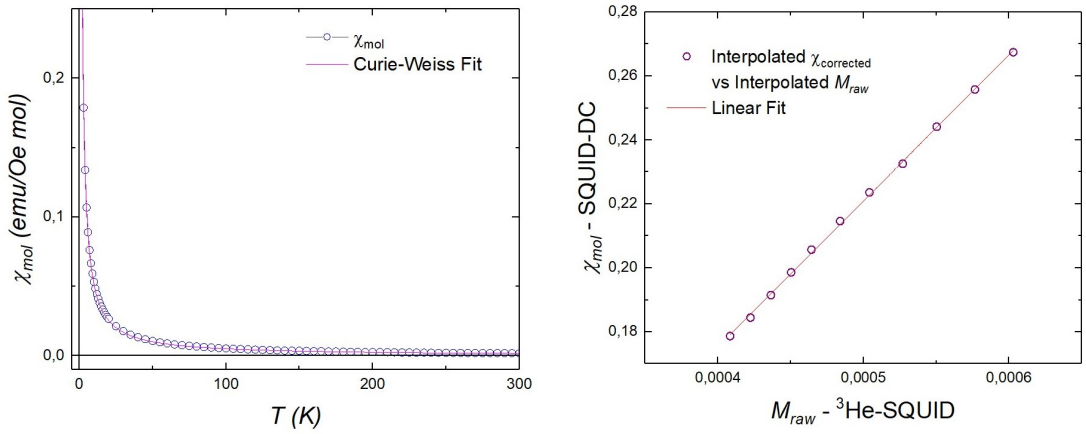

Figure 4.2: a) $\chi - T$ plot after removing the diamagnetic contribution, which provides a $C \approx 0.5\ emuK/Oemol$.b) Linear relation between the interpolated data from the SQUID magnetometer using either liquid Helium and the ^3He cryostats.

thermometer that is located very close to the sample position, which introduces a non-negligible magnetic signal.

We proceeded by interpolating the two sets of data (χ_{mol} with the previous correction for the the 2 K - 300 K range and the raw magnetization M_{raw} for the 0.360 K - 2 K) at the same temperature points in the 2 K - 3 K range.

The relation between the two quantities is $\chi_{mol} = A + BM_{raw-^3He-SQUID}$, which includes a scaling factor and additional additive contributions. The parameters A and B can be derived from the linear fit shown in Figure 4.2 b). By applying this relation to the measured data $M_{raw-^3He-SQUID}$ we obtained χ_{mol} for the 0.360 K - 2 K range temperatures.

4.1.3 Temperature dependent magnetic susceptibility

$(PNP)ZnRu(ox)_3$

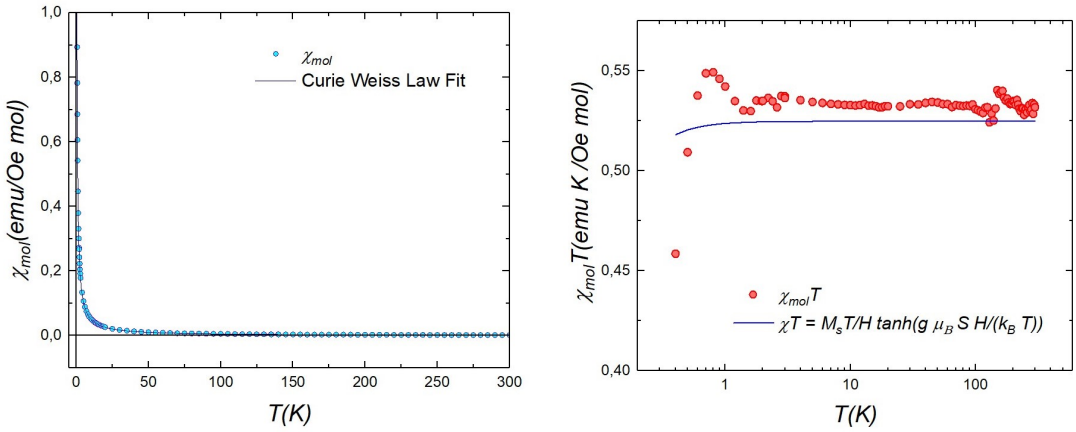

Figure 4.3: (PNP)ZnRu(ox)3 in the 0.360K-300K range

After the whole correction process we can analyze the $(PNP)ZnRu(ox)_3$ data in the full range of temperatures (0.360 K - 300 K).

The χ vs T plot in Figure 4.3 shows a paramagnetic behavior. There is no sign of any phase transitions down to 0.360 K. The Curie-Weiss Law gives $C = 0.52$ emu K/Oe mol. The χT vs T data (Figure 4.3) deviate from the theoretical prediction for a pure paramagnetic system

$$M \approx M_S tanh(\frac{g\mu_B SH}{k_B T}) \longrightarrow \chi T = \frac{M_S T}{H} tanh(\frac{g\mu_B SH}{k_B T}) \tag{4.1.2}$$

that includes the deviations from the simple Curie Law associated with the polarization of the spins by the finite magnetic field. This suggests the existence of weak antiferromagnetic spin-spin interactions. From the Curie constant we can derive also the effective g factor.

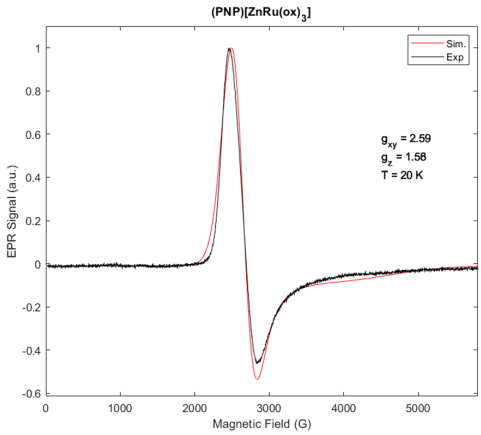

Figure 4.4: EPR

From the relation

$$C = N_A \frac{\mu_B^2 S(S+1) g^2}{3k_B} \tag{4.1.3}$$

we obtain a $g = 2.35$. This result is close to the g value estimated from the fit of Electron Paramagnetic Spectra (Fig. 4.4), which allows determining the principal values of the g-tensor. Indeed, knowing that $g^2 = \frac{1}{3}(g_x^2 + g_y^2 + g_z^2)$, from the EPR data we have $g = 2.30$

Figure 4.5 shows the $1/\chi - T$ plot, which follows a nearly perfect linear relationship. The Weiss temperature is $\Theta = -0.0078K$ which confirms the presence of weak spin-spin interactions.

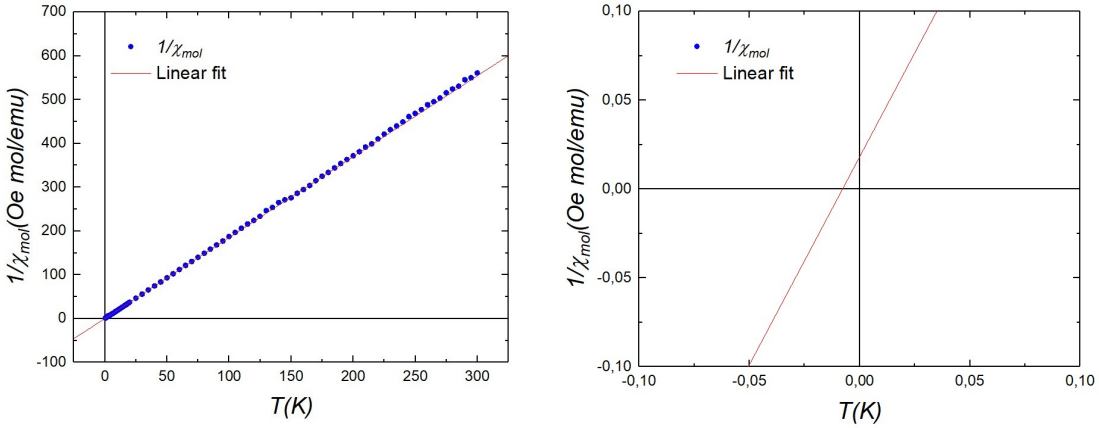

Figure 4.5: $(PNP)ZnRu(ox)_3$ $1/\chi$ vs T plot is showing a almost perfectly linear behavior. From the linear fit we have a $\Theta \approx -0.0078K$

$FeCpRhZn(ox)_3$

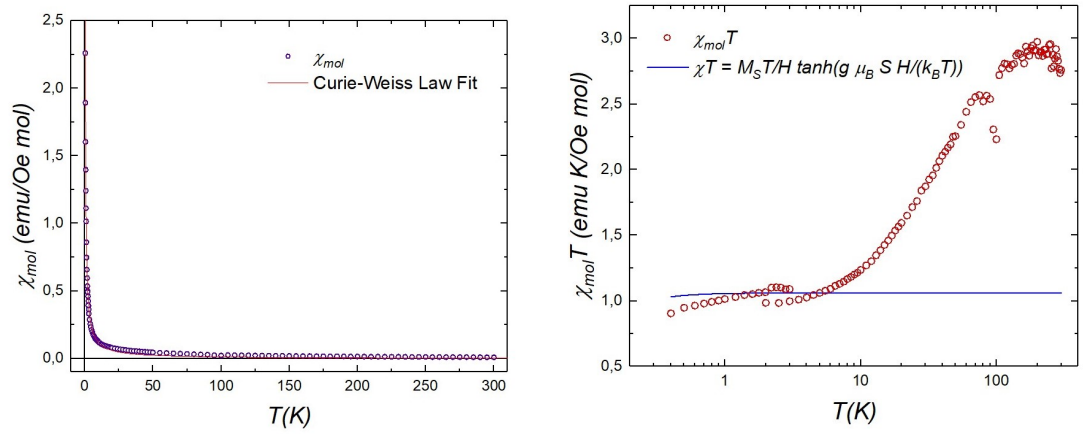

Figure 4.6: Temperature dependence of the magnetic susceptibility of $FeCpRhZn(ox)_3$. a) χ vs T plot follows the Curie-Weiss law, with $C \approx 1.19$ emu K/Oe mol (line). b) χT vs T plot showing the effect of the thermal depopulation of excited spin levels. Below 10 K, each ferrocene molecule behaves as an effective S = 1/2 spin (solid line).

The same correction procedures have been followed for the $FeCpRhZn(ox)_3$. In this section we show the final results of the molar magnetic susceptibility measured in the temperature range of 0.4

- 300 K.

The χ vs T plot (Figure 4.6) shows a behavior with a Curie constant $C \approx 1.19$ emu K/Oe mol. However, the χT vs T plot shows a more complex and interesting behavior (Fig 4.6.It shows a decrease from room temperature, whereas below 10 K it reaches a plateau. In this temperature range, each Fe ion behaves as an effective S = 1/2 system. The theoretical prediction (Eq. 4.1.2), computed with a saturation magnetic moment $M_S = 9.02 \times 10^3$ emu/mol, agrees with the low temperature region. This behavior is typical of ions that have multiple energy levels that become depopulated when T decreases,it is the case with Fe(III) in ferrocene. The change in the Curie constant (or in the effective magnetic moment), is evident also from the $1/\chi - T$ plot in Figure 4.7: it shows a linear relationship but with a deviation at the lowest temperatures. Since the Quantum Spin Liquid state should occur when the Fe ions are in their ground state, we focus our analysis on this region, below approximately 7-10 K, in order to estimate Θ and the effective g.

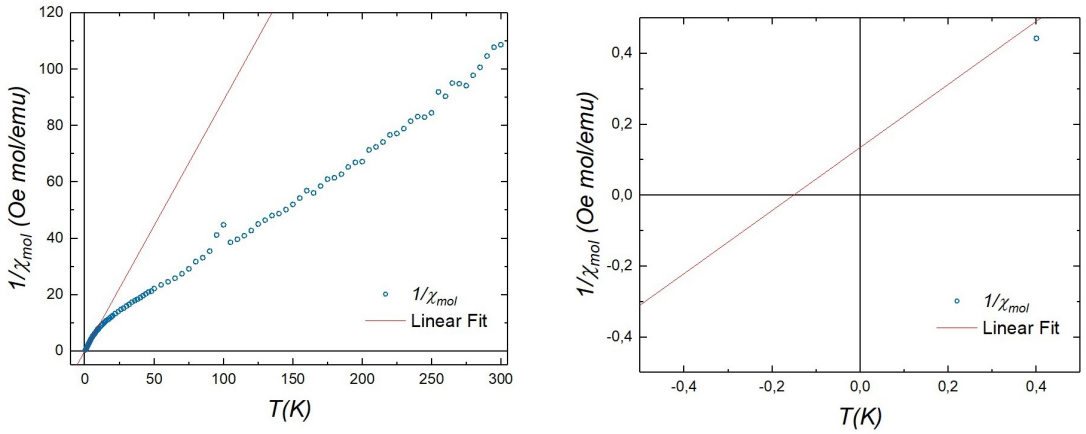

Figure 4.7: $1/\chi$ vs T plot shows a linear behavior with a deviation around 8 K. The linear fit done at the lowest temperatures provides a $\Theta \approx -0.15$ K.

The Curie-Weiss fit provides a Weiss temperature $\Theta \approx -0.15$ K and a Curie constant $C \approx 1.2$ emu K/Oe mol, from which we can compute $g = 3.5$. It lies within the range of g values previously reported for Fe(III) in ferrocene.

4.1.4 Field-dependent magnetization isotherms

The magnetization isotherms measured on both materials are shown in Fig. 4.8. They show the characteristic paramagnetic behavior, with a gradual saturation that can be approximately described with Eq. (4.1.2). The saturation magnetic moment, estimated at the highest magnetic field and for the lowest temperatures allows an independent estimation of the atomic magnetic moments and, thus, of the effective g, which agrees with those obtained from the temperature dependent susceptibility. for both compounds.

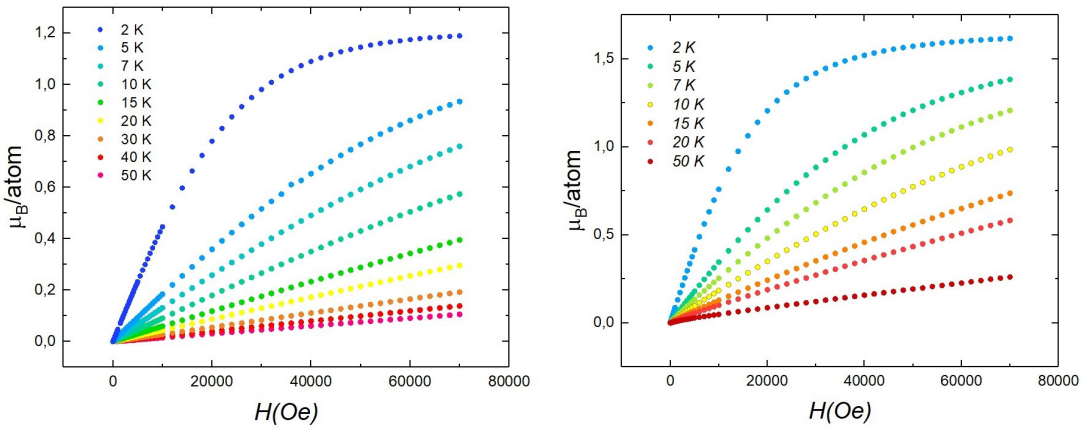

Figure 4.8: Magnetization isotherms of a) $(PNP)ZnRu(ox)_3$ and b) $FeCPRhZn(ox)_3$ at different temperatures

4.2 Specific heat

The specific heat (c_p) was measured from 20 K to 370 mK, and for different magnetic fields (0 T, 2.5 T, 0.5 T, 1 T, 2 T, 3 T and 5 T).

4.2.1 Zero field specific heat

In the following discussion we consider the molar heat capacity at constant pressure c_p divided by the gas constant $R = N_A k_B$. The contribution from the calorimeter and from the grease were estimated from previous calibration measurements and then subtracted in order to obtain the specific heat from the samples.

$(PNP)ZnRu(ox)_3$

We performed measurements on $(PNP)ZnRu(ox)_3$ and on its diamagnetic equivalent $(PNP)ZnRh(ox)_3$, in order to distinguish the heat capacity arising from the spins and the one given by the lattice (Figure 4.9). The two plots coincide above 2 K, as they should, given that at high temperatures only the lattice contribution is visible. Anyway at lower temperatures we were expecting the heat capacity of the magnetic material to be higher than its diamagnetic equivalent but from the measurement it emerges the opposite. Even if the $(PNP)ZnRh(ox)_3$ heat capacity should not exactly follow the Debye law until $T = 0.36$ K, it should drop as temperature does, because the contribution should come just from the lattice vibrations. We attribute this effect to some error in the calibration of the calorimeter used in the measurement of the diamagnetic sample. In fact, data measured on $(PNP)ZnRh(ox)_3$ at high magnetic fields (shown below), give, below 1 K, c_P values about one order of magnitude smaller than those measured in the diamagnetic sample.

Despite these experimental limitations, we conclude that the spin-spin interactions in this system

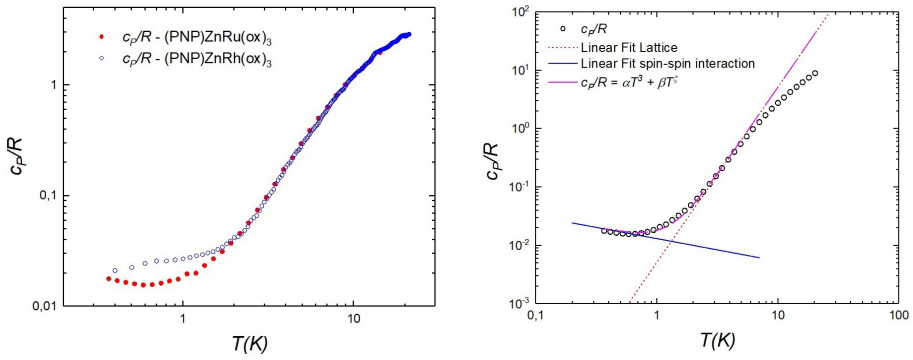

Figure 4.9: a) Specific heat of $(PNP)ZnRu(ox)_3$ and of its diamagnetic derivative $(PNP)ZnRh(ox)_3$ measured at $B = 0$. b) Fit of the data measured on $(PNP)ZnRu(ox)_3$ based on a contribution proportional to T^3, associated with lattice vibrations, plus an $\beta T^{-\xi}$ term, which could arise from spin-spin interactions.

are too weak to give a very significant contribution in the temperature range accessible to our experiments. This is compatible with the very low Weiss temperature found in the previous section.

In order to estimate this contribution, we have followed a different approach. From the $(PNP)ZnRu(ox)_3$ c_P plot at $B = 0$ T (Figure 4.9) we made a linear fit between 2K and 5K in order to derive the parameter α of the Debye model for the lattice specific heat $\frac{c_p}{R} = \alpha T^3$. We find $\alpha = 5.19 \times 10^{-3} K^{-3}$. Then, we have found a reasonably good fit of the $(PNP)ZnRu(ox)_3$ heat capacity using the expression

$$c_P = \alpha T^3 + \beta T^{\xi} \tag{4.2.4}$$

which is plotted in Figure 4.3 b). Notice that the term βT^{ξ}, representing the spin-spin interaction, has the exponent $\xi = -0.39$. According to the Kitaev-Heisenberg model introduced in the theoretical chapter, a system showing a Quantum Spin Liquid phase is expected to follow a power law different from T^{-2}.

$FeCpRhZn(ox)_3$

The diamagnetic equivalent of $FeCpRhZn(ox)_3$ is the $CoCpRhZn(ox)_3$. Their zero-field specific heats are shown in Figure 4.10 a).

In this case, the heat capacity measured for the diamagnetic equivalent is lower than than our sample, although it still does not decrease as we would have expected. For the same reasons, it would not be reliable to subtract these experimental data from the $FeCpRhZn(ox)_3$. Qualitatively, the spin-spin interactions seem to be stronger here, but still we need to go at lower temperatures to quantify them. Again, this is compatible with the larger Weiss temperature found for this complex as compared to $(PNP)ZnRh(ox)_3$.

Following the same steps as before, we derive the parameters $\alpha = 6.19 \times 10^{-4} K^{-3}$, $\beta = 0.103$ and $\xi = -1.048$ (Figure 4.10 b)). Also in this case the heat capacity follows a power law different from T^{-2}, which is a clue for a system with a Quantum Spin Liquid phase.

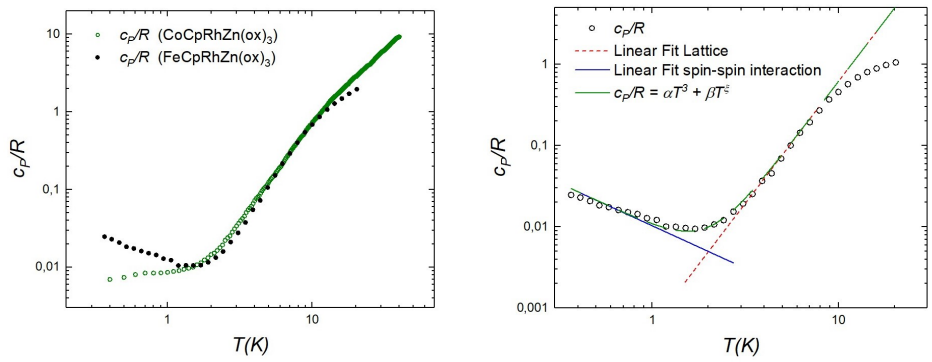

Figure 4.10: a) cP/R vs T plot at zero field for $FeCpRhZn(ox)_3$ and $CoCpRhZn(ox)_3$. b) $FeCpRhZn(ox)_3$ $c_P - T$ plot at $B = 0$ and linear fit to derive the parameters α, β and ξ.

4.2.2 Magnetic field dependence of the specific heat

Specific heat data measured for both compounds at different magnetic fields are shown in Figs. 4.11 and 4.12. The effect of the field is to split the spin-up and spin-down levels. This gives rise to a clear Schottky-like anomaly, with a maximum temperature that increases with increasing B. We apply Equation 3.1.3 in order to determine the energy gap $T_\Delta = \frac{\Delta}{k_B}$ for every magnetic field. For this, we defined a function that involves the Schottky bump and the Debye model, with the α found previously:

$$\frac{c_p}{R} = \frac{T_\Delta^2}{T^2}\left(e^{T_\Delta/2T} + e^{-T_\Delta/2T}\right)^{-2} + \alpha T^3 \tag{4.2.5}$$

The term T_Δ parametrizes the energy gap associated with the average local field seen by the spins.

By plotting every T_Δ vs B we can compute the average effective g and the zero field energy excitation gap $T_0 = 0.10$ associated with the spin-spin interactions. We find $g \simeq 2.082$ and $T_0 \simeq 0.1$ K for $(PNP)ZnRh(ox)_3$ and $g \simeq 2.31$ and $T_0 = 0.11$ K for $FeCpZnRh(ox)_3$.

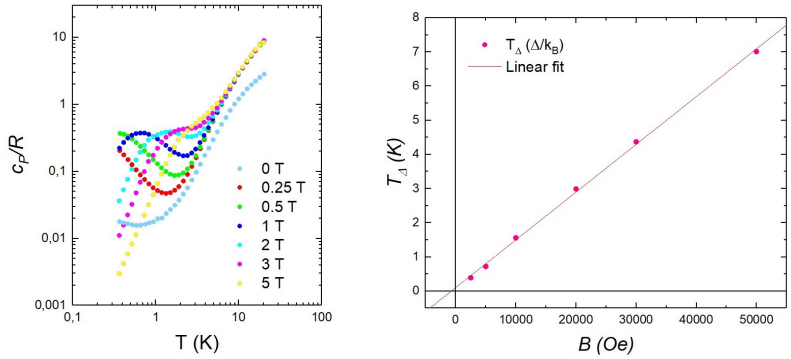

Figure 4.11: $(PNP)ZnRu(ox)_3$ a) Heat capacity vs T at different magnetic fields. b) T_Δ points derived for every B and linear fit.

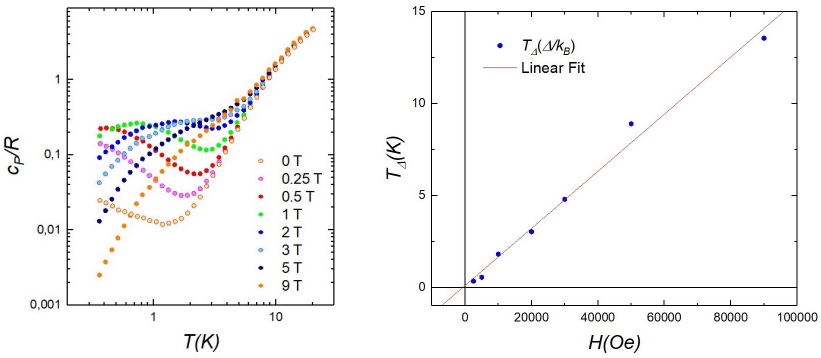

Figure 4.12: $FeCpRhZn(ox)_3$ a) Heat capacity vs T at different magnetic fields. b) T_Δ points derived for every B and linear fit.

In both cases the g parameters are smaller than those derived from the magnetization analysis. The fitting process with the function defined in Eq. 4.2.5 presented some problems, especially for higher fields (5 T and 9 T), so some errors should be taken into account.

For both materials, we find $T_0 \neq 0$ for $B = 0$. However, the values are very low, smaller than our lowest experimental temperature. Therefore, these results confirm the indications obtained from the Weiss temperatures: that spin-spin interactions are present in both systems but also that they are very weak.

4.3 Discussion: relevance for the existence of a QSL phase

We can compute the *frustration ratio* defined as $f = \frac{T_0}{T_{min}}$, where $T_{\min}$ is the lowest accessible temperaure for which the systems remain paramagnetic. In our case, $T_{\min} \simeq 0.35$ K. Then, $f < 1$ in both cases ($f = 0.28$ for $(PNP)ZnRu(ox)_3$ and $f = 0.31$ for $FeCpRhZn(ox)_3$) because T_{min} is still too high. In other words, it is not surprising that no long-range magnetic order is observed at temperatures that are higher than the typical strength of the spin-spin interactions. It is then necessary to study both the magnetic moment and the heat capacity at temperatures below 0.1 K in order to draw more definite conclusions about the QSL phase. Moreover, measuring the heat capacity at lower temperatures could allow us to see if the two peaks behavior emerges, as predicted by the Kitaev - Heisenberg model, and to compute the entropy of each spin. Still, some indications point to an unusual paramagnetic behaviour, like the exponent of the $B = 0$ specific heat. Also, the fact that the spin-spin interactions are found to be significantly weaker for the $(PNP)ZnRh(ox)_3$ are compatible with the predominance in this system of Kitaev interactions. For oxalate layers, it has been predicted that the superexchange interactions between ions with very strong spin-orbit interaction should lead to a close to complete suppression of the "conventional" exchange and superexchange interactions. This would lead to a smaller net interaction between the Ru spins, as we have observed, but would also mean that this system might provide a more pure realization of the Kitaev model, albeit at very low-T.

CHAPTER 5

Conclusions

The goal of this work was to experimentally characterize, through magnetization and heat capacity measurements, two novel molecular materials, $(PNP)ZnRu(ox)_3$ and $FeCpRhZn(ox)_3$, in order to understand if they could be two good candidates for *Quantum Spin Liquids*. The guideline that we followed during our research can be summarized in three key points: the absence of long-range magnetic order, the presence of spin-spin interaction and the compatibility of experimental parameters with the *Kitaev-Heisenberg Model*.

By measuring the temperature dependence of the magnetic susceptibility χ, we verified the absence of long-range magnetic order down to 360 mK for both materials. This conclusion is supported by the absence of sharp peaks or discontinuities in the temperature dependence of the heat capacity c_P.

Still, the same results, supported by heat capacity data, suggest the presence of antiferromagnetic interactions. However, the interactions are also very weak, thus it is still not surprising that the two systems remain paramagnetic even down to 350 mK.

By studying the temperature dependence of the experimental heat capacity at zero field, we found that its behavior at low temperatures can be modeled as $c_P \propto \beta T^{\xi}$, where $\xi \neq -2$. This result is consistent with the *Kitaev-Heisenberg model* predictions, in particular with the existance of spin excitations different from spin flips.

The results obtained so far appear promising and are they are compatible with a QSL physics. They need to be extended to very low T, so that $k_B T \ll J$, the scale of spin-spin interactions.

Besides, during this research, certain uncertainties and limitations have emerged that need to be addressed to achieve more accurate estimates. A deeper study of the heat capacity could be done

if we could properly remove the lattice contribution below 7 K. In this way it could be possible to isolate the spin-spin interactions contribution to c_P, observe if the heat capacity shows the two peaks at T_L and T_H and measure the value of the entropy between them.

Bibliography

[1] Stern, A. and Lindner, N. H. (2013) Topological Quantum Computation—From Basic Concepts to First Experiments. *SCIENCE,* **339**, 1179.

[2] Román-Roche, J., Luis, F., and Zueco, D. (Oct, 2021) Photon Condensation and Enhanced Magnetism in Cavity QED. *Phys. Rev. Lett.,* **127**, 167201.

[3] Sankar Das Sarma, M. F. and Nayak, C. (2015) Majorana zero modes and topological quantum computation. *Nature, npj Quantum Information,* **1**.

[4] Tsvelik, A. M. (2014) Quasiparticle Signatures in Quantum Spin Liquids. *Physics,* **7**.

[5] Knolle, J., Kovrizhin, D. L., Chalker, J. T., and Moessner, R. (May, 2014) Dynamics of a Two-Dimensional Quantum Spin Liquid: Signatures of Emergent Majorana Fermions and Fluxes. *Phys. Rev. Lett.,* **112**, 207203.

[6] Burzurí, E., Martínez-Pérez, M. J., Martí-Gastaldo, C., Evangelisti, M., Mañas-Valero, S., Coronado, E., Martínez, J. I., Galan-Mascaros, J. R., and Luis, F. (2023) A quantum spin liquid candidate isolated in a two-dimensional CoIIRhIII bimetallic oxalate network. *Chem. Sci.,* **14**, 3899–3906.

[7] Balents, L. (2010) Spin liquid in frustrated magnets. *Nature,* **464**.

[8] Alonso, I. G. Quantum circuits based on artificial magnetic molecules PhD thesis Zaragoza University (2023).

[9] Diez, D. G. Qudits Moleculares de Espín Acoplados a Circuitos Superconductores. Master's thesis Zaragoza University (2023/2024).

[10] Ashcroft, M. Solid State Physics chapter 31. Diamagnetism and Paramagnetism Cengage (1976).

[11] Evangelisti, M., Luis, F., de Jongh, L. J., and Affronte, M. (2006) Magnetothermal properties of molecule-based materials. *J. Mater. Chem.,* **16**, 2534–2549.

[12] Ashcroft, M. Solid State Physics chapter 23. Quantum Theory of the Harmonic Crystal Cengage (1976).

[13] Callen, H. B. Thermodynamics and an introduction to thermostatistics chapter 15.3 Wiley second edition edition (1985).

[14] Ashcroft, M. Solid State Physics chapter 32. Electron Interactions and Magnetic Structure Cengage (1976).

[15] Kitaev, A. (2006) Anyons in an exactly solved model and beyond. *Annals of Physics,* **321**(1), 2–111 January Special Issue.

[16] Yamaji, Y., Suzuki, T., Yamada, T., Suga, S.-i., Kawashima, N., and Imada, M. (May, 2016) Clues and criteria for designing a Kitaev spin liquid revealed by thermal and spin excitations of the honeycomb iridate Na_2IrO_3. *Phys. Rev. B,* **93**, 174425.

[17] Nasu, J., Udagawa, M., and Motome, Y. (Sep, 2015) Thermal fractionalization of quantum spins in a Kitaev model: Temperature-linear specific heat and coherent transport of Majorana fermions. *Phys. Rev. B,* **92**, 115122.

[18] Yamada, M. G., Fujita, H., and Oshikawa, M. (Aug, 2017) Designing Kitaev Spin Liquids in Metal-Organic Frameworks. *Phys. Rev. Lett.,* **119**, 057202.

APPENDIX A

Mass correction and diamagnetic contribution

A.1 Diamagnetic contribution

In order to characterize correctly the material $(PNP)ZnRu(ox)_3$, the diamagnetic contribution has to be removed.

Since

$$\chi_{measured} = \chi_{ZnRu} + \chi_{diamagnetic} \tag{A.1.1}$$

and keeping into account that

- $\chi_{diamagnetic}$ can be considered temperature independent;
- $\chi_{ZnRu} = \frac{C}{T}$, where C is the Curie constant;
- $\chi = \frac{M}{H}$ (with $H = 10^3$ Oe);

it follows that

$$M_{measured}T = CH + M_{diamagnetic}T \tag{A.1.2}$$

Plotting MT vs T and fitting the curve (Figure A.1), the angular coefficient corresponds to the diamagnetic contribution to the total magnetization: $M_{diamagnetic} = -2.04\text{x}10^{-6}$ emu.

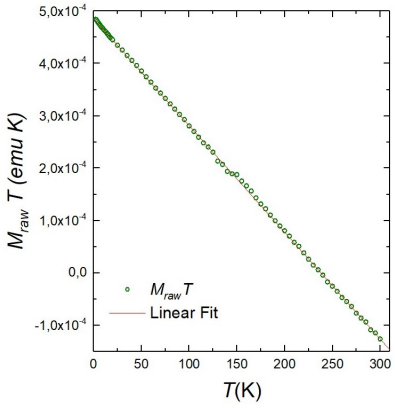

Figure A.1: MT vs T Linear fit

A.2 Re-estimation of sample mass

Now we show the procedure to refine the mass of the sample from the data collected.

For an ideal paramagnet:

- Curie Law: $\chi_{mol} = \frac{C}{T} \approx n\frac{g_{eff}^2\mu_B^2 S(S+1)}{3k_BT}$ for $k_BT >> g_{eff}\mu_B H$
- $M \approx ng_{eff}\mu_B J tanh(\frac{g_{eff}\mu_B SH}{k_BT})$ for $J = 1/2$

If the measured mass and the estimated one are equal, we should have $n = N_A$.

For $k_BT << g_{eff}\mu_B SH$, $M_S \approx ng_{eff}\mu_B S$.

If we take the ratio:

$$\frac{C}{M_S} = \frac{ng_{eff}^2\mu_B^2 S(S+1)/3k_B}{ng_{eff}\mu_B S} \quad \rightarrow \quad g_{eff} \approx \frac{2Ck_B}{M\mu_B} \approx 2.38 \tag{A.2.3}$$

We derived $C = 4.846 \times 10^{-7}$ emu K/Oe $= 4.808 \times 10^{-3}$ emu K/T from the $\chi T - T$ plot of the raw data and the value of $M_S = 0.00607$ emu from the $MvsH$ plot.

Using the new $g_{eff} = 2.38$ we can estimate the molar saturation magnetic moment $M_{molar} = N_A g_{eff}\mu_B S = 6.65 \times 10^3$ emu/mol.

Knowing that $\frac{M_{raw} * m_{molar}}{m} = M_{mol}$ (the molar weight $m_{molar} = 1054.02 g/mol$), the sample mass is $m = \frac{M_{raw} m_{molar}}{M_{mol}} = 0.963 mg$, where M_{raw} is the total saturation raw magnetic moment used before.

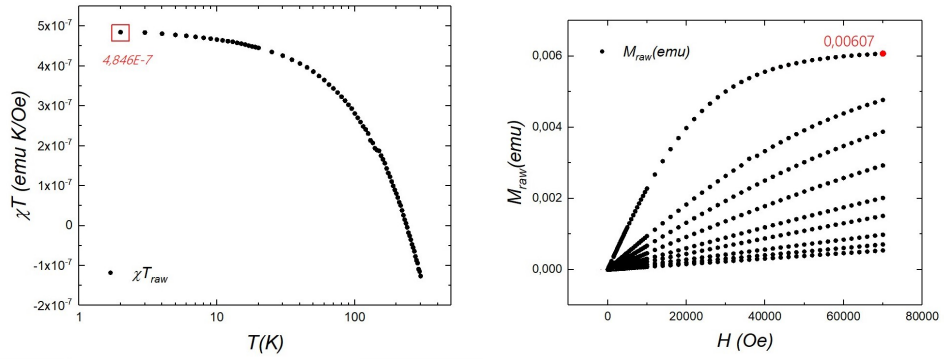

Figure A.2: Caption

APPENDIX B

Estimation of the grease's mass

One could also use the diamagnetic contribution to estimate the mass of the grease.

The diamagnetic susceptibility per unit of mass of the grease is known: $\chi_d = -1.015\text{x}10^{-6}\frac{emu}{gOe}$.

If we associate all the diamagnetic noise to the grease we have:

$$m_{grease} = \frac{2.04 \times 10^{-6} emu}{H\chi_d} \approx 2.01mg \tag{B.0.1}$$

which is very different from the one measured $m = 2.79$ mg.